Magnetostructural phase transition in electroless-plated Ni nanoarrays

Chun-Chao Huang, Chih-Chieh Lo, Yuan-Chieh Tseng, Chien-Min Liu, and Chih Chen

---

Articles you may be interested in

Exchange bias beyond the superparamagnetic blocking temperature of the antiferromagnet in a Ni-NiO nanoparticulate system
J. Appl. Phys. **115**, 073904 (2014); 10.1063/1.4866196

Core/shell magnetism in NiO nanoparticles
J. Appl. Phys. **114**, 083906 (2013); 10.1063/1.4819807

Sharp variation in coercivity and magnetic interactions in patterned CoxNi1x nanoarrays
J. Appl. Phys. **114**, 063902 (2013); 10.1063/1.4817866

Self-ordered magnetic -FeSi2 nano-stripes on Si(111)
Appl. Phys. Lett. **102**, 251604 (2013); 10.1063/1.4812239

Coupled microstructural and magnetic transition in Co-doped Ni nano-arrays
J. Appl. Phys. **110**, 073913 (2011); 10.1063/1.3647753

Magnetostructural phase transition in electroless-plated Ni nanoarrays

Chun-Chao Huang, Chih-Chieh Lo, Yuan-Chieh Tseng,[a] Chien-Min Liu, and Chih Chen
Department of Materials Science & Engineering, National Chiao Tung University 1001, Ta Hsueh Road, Hsin-Chu 30010, Taiwan

Ni nanoarrays were synthesized by electroless-plating and shaped by an anodic aluminum oxide template. The as-plated arrays exhibited superparamagnetic (SM) ordering resulting from nanocrystalline microstructure. Ferromagnetic (FM) ordering was found to be restored as the arrays' crystallinity was enhanced upon post-annealing. The microstructure (crystallinity) and the FM ordering are strongly coupled, revealing a magneto-structural correlation for the arrays. The magnetostructural properties of the arrays can be controlled by post-annealing, where the magnetization is proportional to the annealing temperature. The electroless-plated arrays synthesized in this work display magnetic anisotropy not found in electroplated ones. This is likely attributed to the nature of the clusterlike microstructure, whose cluster-boundaries may confine the FM rotation within the cluster. The spin-polarization was probed by x-ray magnetic circular dichroism while the arrays underwent the SM→FM phase transition. The sum-rules results reveal that the total magnetization of the arrays is dominated by spin moment (m_{spin}). The change in m_{spin} is responsible for the SM→FM phase transition upon annealing, as well as for the loss of magnetization upon temperature increase that we observed macroscopically. © *2011 American Institute of Physics*. [doi:10.1063/1.3594692]

I. INTRODUCTION

In a world of magnetic materials, superparamagnetism usually appears in small ferromagnetic (FM) particles with a diameter ranging from 1 to 10 nm.[1,2] Superparamagnetism undermines the applications of magnetic materials, because the materials no longer possess net magnetization and become more difficult to modify and control. The occurrence of superparamagnetism is accompanied by a sudden loss of magnetization along with a paramagneticlike behavior. The transformation to an FM phase from a superparamagnetic (SM) phase requires the recovery of FM coupling strength, which is intimately connected to a material's spin-polarization. How to remove the SM in low-dimensional materials has been a long-standing but important task.[3,4] A better understanding of the SM→FM magnetic phase transition[5] in nanostructures is essential for advancing magnetism-related technologies.

Electroless-plating is an auto-catalytic process composed of several simultaneous reactions in an aqueous condition, which due to its simplicity in operation has been widely applied in electronics, automotive, aerospace, and other industries.[6–8] However, due to the absence of current to assist material's growth, electroless-plating tends to result in poorer material crystallinity than does electroplating. Recently, the SM phase was discovered in electroless-plated Ni nanoarrays.[9,10] The suppression of FM ordering was attributed to the nanosized crystallites naturally formed during the deposition. It was found that the FM ordering can be restored when the arrays' crystallinity was enhanced upon annealing.

Despite the discovery of the SM→FM phase transition, the mechanism leading to the emergence of the FM ordering from within the SM ground state is not fully understood. For example, the macroscopic magnetization is composed of spin (m_{spin}) and orbital (m_{orb}) moments. The individual contributions of these two quantities upon the SM→FM phase transition are invaluable but, have not been revealed. Thus, m_{orb} and m_{spin} were decoupled using x-ray magnetic circular dichroism (XMCD) and the electronic structure was probed using x-ray absorption spectroscopy (XAS). Moreover, since the magnetic ordering is highly dependent on the crystallinity, a systematic study of the magneto-structural correlation is necessary to further understand how microstructural ordering affects the magnetic properties, such as magnetization and magnetic anisotropy. This work explores the SM (nanocrystalline)→FM (polycrystalline) phase transition for electroless-plated Ni arrays and provides insights into how spin-polarization and microstructure influence the phase transition, key to understanding the complex magnetic behaviors.

II. EXPERIMENTAL

An anodic aluminum oxide (AAO) template with pores of about 70 nm in diameter was prepared on a p-type Si substrate by following the process described in Ref. 8. The AAO-Si sample was first sensitized by an $SnCl_2$/HCl solution (40 g/L $SnCl_2$ + 3 ml/L HCl) and then activated by a $PdCl_2$/HCl solution (0.15 g/L $PdCl_2$ + 3 ml/L HCl).[6,9] This reduced Pd^{+2} to Pd, serving as a nucleation center for the deposition of Ni atoms. The electroless-plating solution used in this work was composed of the main Ni source $NiSO_4$, the reducing agent NaH_2PO_2, the stabilizing agent $Na_2C_4H_4O_4$, and the buffer agent $Pb(NO_3)_2$. The pH and environmental temperature for the deposition were set at 5.0 and 65 °C,

[a] Author to whom correspondence should be addressed. Electronic mail: yctseng21@mail.nctu.edu.tw.

109, 113905-1

respectively, in order to mirror C. Liu *et al.*[9] who demonstrated the superparamagentic behaviors seen in the as-plated sample fabricated with such conditions. Finally, the AAO was removed by bathing the samples in an NaOH solution, leaving the arrays rooted perpendicularly on the Si.

One of the three Ni nanoarray samples investigated in this work was as-plated, another was post-annealed at 350 °C for 30 min using a thermal furnace (TF),[11] and a third was post-annealed at 400 °C for 2 min using a rapid thermal annealing (RTA) facility. Both post-annealed samples were in a vacuum condition with the presence of the AAO. For the TF case, temperature was increased to 350 °C in 20 min and then maintained for 30 min. For the RTA case, temperature was raised to 400 °C in 10 s and maintained for 2 min. The arrays' surface morphology was probed using a scanning electron microscope (SEM, JSM 6500 F, operated at 15 keV). A transmission electron microscope (TEM, JEM-2100 F, operated at 200 keV) was used to probe the microstructure and diffraction pattern. The composition of the arrays was determined by energy-dispersive x-ray spectrometry (EDX). The magnetic hysteresis (M-H) curves were identified by a superconducting quantum interference device (SQUID) magnetometer at 30 K, along arrays' long and short axes. We found that the plain Si substrate displays countable diamagnetism.[12] Thus, the M-H curves shown in this work exclude Si's contribution. X-ray absorption spectra (XAS) were collected over Ni L_2 and L_3 edges with total electron yield mode (TEY) at beamline 11 A of National Synchrotron Radiation Research Center (NSRRC), Taiwan. XMCD signals were collected along with XAS with opposite x-ray helicities to probe the spin-polarization state of the arrays. XMCD signals were taken at various temperatures (30∼55 K) along the arrays' long and short axes, all under an applied field of 1 T. Due to the cryostat's cooling limitation, the lowest achievable temperature was ∼30 K for XMCD measurements. This consequently set the quantitative comparison for SQUID and XMCD to be at 30 K in this work. The short-axis XMCD measurement was defined at an incident x-ray angle of 30° with respect to the in-plane direction of the Si substrate. Afterwards, sum-rules analysis[13,14] was applied to the XAS and XMCD spectra to estimate m_{orb} and m_{spin}.

III. RESULTS AND DISCUSSION

Figure 1(a) shows the SEM image of Ni nanoarrays after the removal of the AAO. Its orientation was nearly perpendicular, and the arrays on the Si substrate were freestanding. The set of arrays was ∼350 nm in height and ∼70 nm in diameter (aspect ratio = ∼5). The three samples investigated in this work were all set to be with such dimension by the AAO template. The uniform structural configuration thanks to the assistance of the AAO template during electroless plating. Figure 1(b) is the top-view TEM image for the arrays prior to the removal of the AAO. The arrays are composed of clusters that commence growth along the AAO walls and merge at the center of the AAO pores. The details of the cluster structures appear in the arrays' cross-sectional TEM image, Fig. 1(c). The TEM indicates that the cluster structures are isolated. The growth of the arrays was well con-
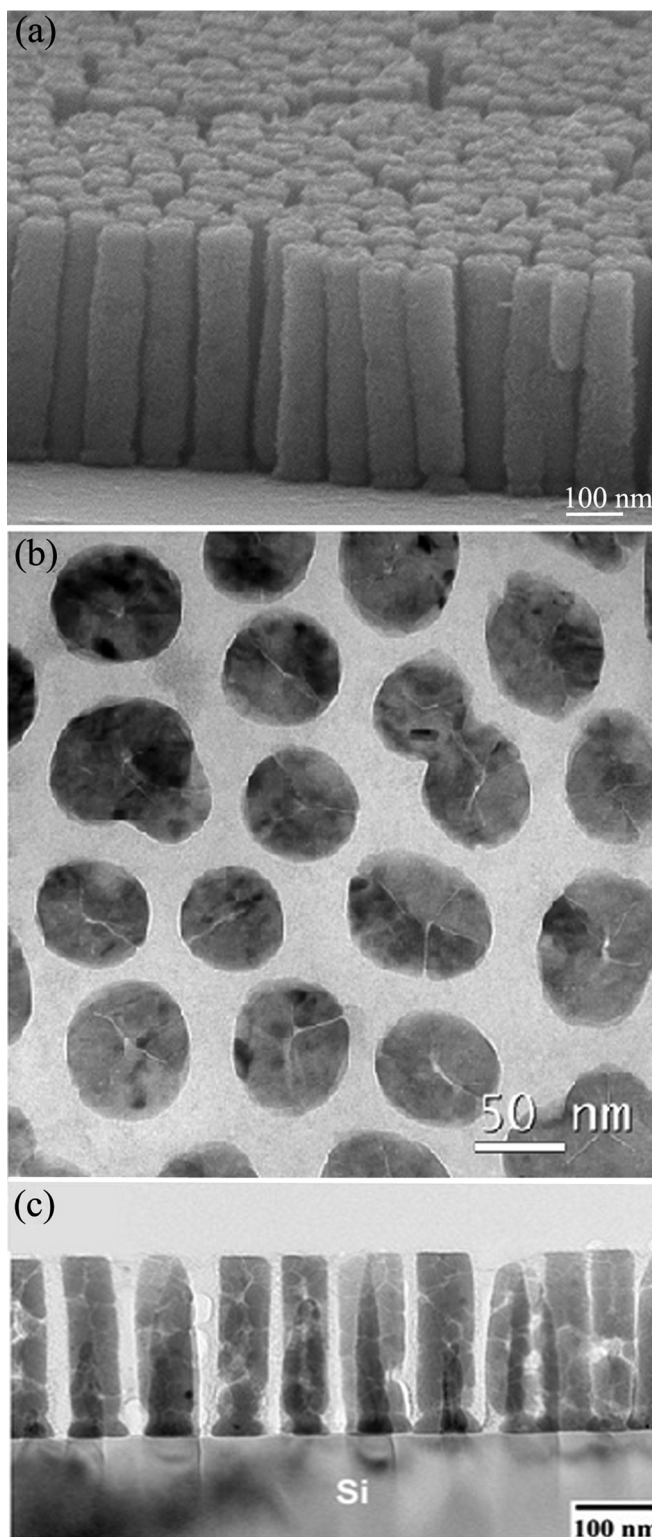

FIG. 1. (a) SEM image of the Ni arrays freestanding on a Si substrate. (b) Top-view TEM image of the Ni arrays, where the arrays are covered by the AAO. (c) Cross-sectional view TEM image of the Ni arrays.

fined by the AAO during the plating process, and we found that the annealing temperature only varied the microstructure and magnetism of the arrays, as discussed in the following, but did not change the shape or structural configuration of the arrays.

Figures 2(a), 2(b), and 2(c) present the diffraction patterns for the as-plated, 350 °C-30-min,[11] and 400 °C-2-min
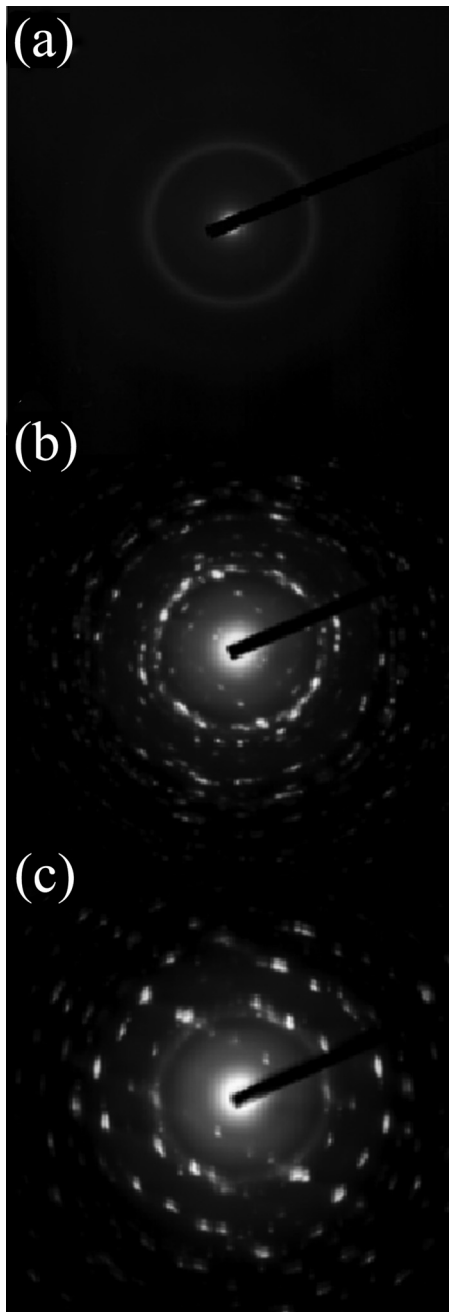
FIG. 2. Diffraction patterns of (a) as-plated, (b) 350 °C-30-min and (c) 400 °C-2-min Ni arrays.

samples, respectively. The diffraction patterns were taken from top view [Fig. 1(b)] with an aperture covering at least 30 arrays to assure that the crystallinity was well-represented. For Fig. 2(a), the diffusive ring corresponding to Ni {111} planes confirms the existence of the nanocrystalline structure with crystallites 2~3 nm in diameter.[9] After post-annealing, the diffraction pattern changes from ring to spots, indicating the microstructure's transforming from nanocrystalline[15] to polycrystalline[16] as a result of crystallinity enhancement. The 400 °C-2-min sample exhibits more evident spots than the 350 °C-30-min sample, suggesting that the former has more defined crystallographic planes as well as a better crystallinity. It also reveals that the crystallinity is more dependent on annealing temperature than on annealing time.

Figure 3 demonstrates the M-H curves for the three samples with magnetic field applied along the arrays' long [Fig. 3(a)] and short [Fig. 3(b)] axes. The as-plated sample displays much less magnetization than the other two, which is attributed to the SM phase as reported previously.[9] The SM phase of the as-plated sample is verified by the sample's temperature-dependent M-H curves, as presented in Fig. 4(a). At low temperature, the sample displays FM-like behaviors featuring measurable coercive field (H_c) and remnant magnetization (M_r). These features gradually disappear as temperature increases, with the M-H finally becoming more linear at 10 K, implying that the sample's magnetic ordering is sensitive to thermal instability, which is typical of the SM phase. We also present zero-field cooling (ZFC) and field-cooling (FC) data of the as-plated sample in Fig. 4(b). It can be seen that the blocking temperature (T_B) of the sample is about ~5 K (lower inset). The SM nature can also be verified by fitting the Langevin equation[17,18] above T_B, and the fitting result agrees well with the experimental data, as demonstrated in the upper inset of Fig. 4(b). After post-annealing, the FM ordering is gradually restored. The FM restoration is highly dependent on the level of crystallinity, demonstrating a significant coupling between the FM ordering and the microstructure. The hysteretic M-H curves of the post-annealed samples indicate the formation of FM domains, which developed simultaneously with the crystallinity enhancement.
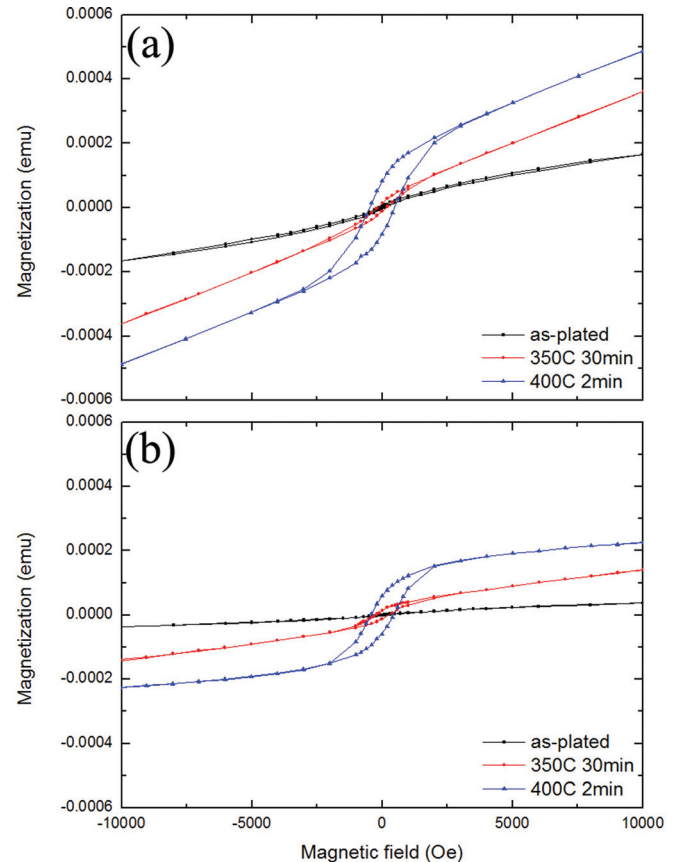

FIG. 3. (Color online) M-H curves for the three samples with magnetic field applied along the arrays' (a) long and (b) short axes. Data were collected at T = 30 K.
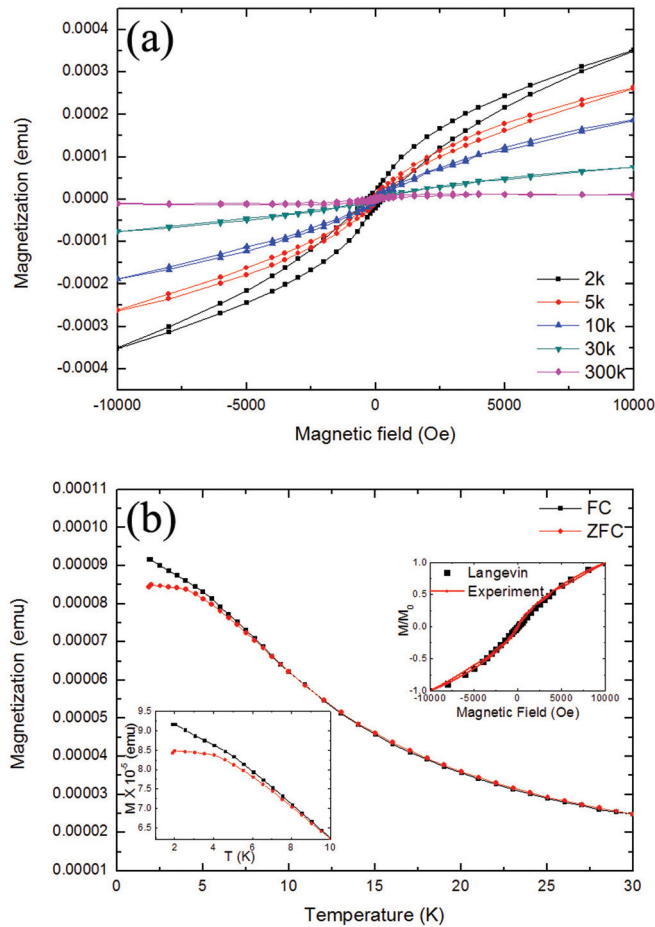
FIG. 4. (Color online) (a) Temperature-dependent M-H curves for the as-plated Ni arrays. Data were taken along the array's long axis. (b) Main panel: ZFC and FC (15 000 Oe) measurements as a function of temperature. ZFC and FC data were taken along the arrays' short axis. Lower inset: enlarged ZFC and FC data around $T_B = 5$ K. Upper inset: experimental data and Langevin fitting for 30 K. Details of Langevin fitting are described in Ref. 18.
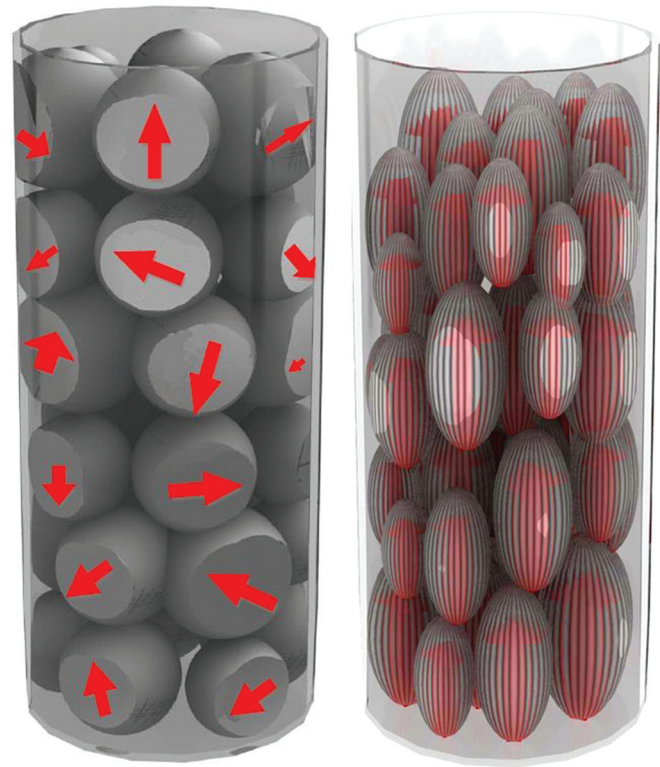

FIG. 5. (Color online) Schematic comparison between electro-plated (right) and electroless-plated (left) arrays' microstructures. The illustrations were made based on the TEM results of Ref. 20 (electro-plating) and of Fig. 1(c) (electroless-plating) in this work. Red arrows represent the magnetic moments.

The striking correlation between the FM ordering and the crystallinity is attributed to the nature of electroless plating. We observed that manufacturing nano-array/wire structures using electro-plating tends to produce segmented polycrystalline structures parallel to the array/wire's long axis.[19,20] This is because the plating is triggered at the electrode side and followed by growth along the long axis, due to the space confinement of the array/wire. This mechanism is likely to result in high material-homogeneity throughout the array. However, without current-assistance, poor material-homogeneity and low crystallinity are expected for the electroless-plated arrays. The schematic comparison in Fig. 5 between electroplated and electroless-plated arrays' microstructures illustrates their microstructural differences. The low crystallinity can be thought of as a type of micro-structural disordering, which tends to frustrate the magnetic ordering. For the as-plated sample, its structural ordering is short-range, only seen in a crystallite with a diameter of 2~3 nm. Such small particles tend to have unstable FM moments and be far apart, making them easily affected by thermal instability, which is inherent to the SM phase (Fig. 4). However, we found that heat treatment restores the FM ordering

by enhancing the microstructural ordering, leading to the SM→FM phase transition. This phase transition can be therefore characterized as a magneto-structural type. It refers to simultaneous developments of the FM ordering and of the microstructural ordering. Physically, the development of the microstructural ordering favors the growth of FM crystallites, which stabilizes the FM coupling that can withstand the thermal instability.

We found that our 400 °C-2-min sample carries magnetization of $\sim 4 \times 10^{-4}$ emu at 1 T, which is about one order less than that of the electroplated samples.[21] Although the discrepancy may be resulted from different sample volume/weight between our measurements and others, it could also be due to the Ni$_3$P (Ref. 22–24) and partial NiO phases [Fig. 6(a)], which are likely to frustrate the FM ordering of our sample. When the Si's diamagnetism is excluded, the magnetization is not saturated along the long axis at high field (>13 000 Oe), and the short axis tends toward greater saturation and moment alignment than the long axis. This is different than electroplated array/wire structured materials, whose moment saturations along long axis were usually found to be smaller than 5000 Oe.[25,26] The electroless-plated arrays' intriguing magnetic anisotropy can be again correlated to their microstructure. The electroless-plating may stimulate material's growth wherever nucleation energy is low, because of the absence of current-assistance. The TEM results [Figs. 1(b) and 1(c)] imply that the AAO wall provides a heterogeneous nucleation location for the deposition
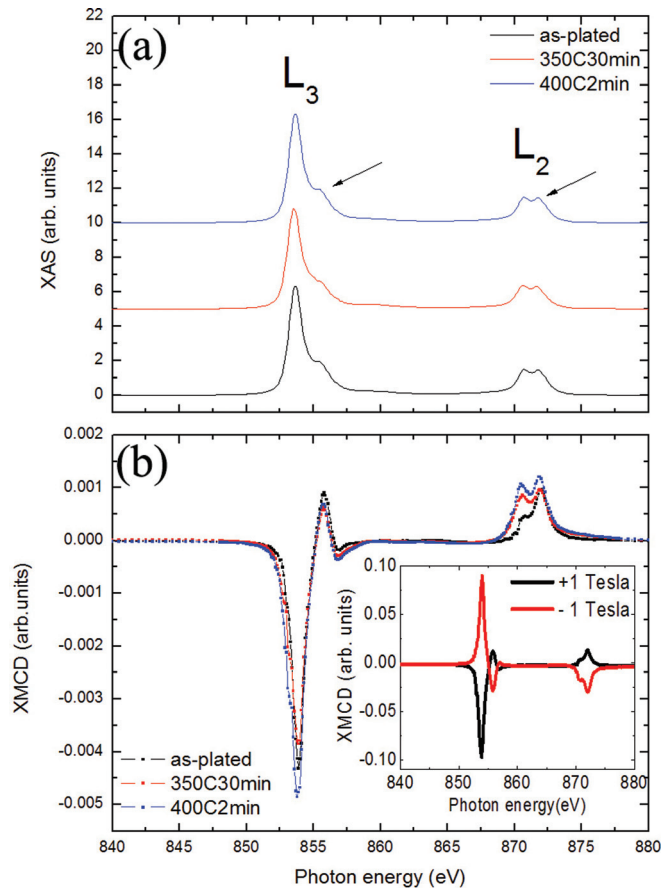
FIG. 6. (Color online) Ni $L_{2,3}$ edges (a) XAS and (b) XMCD for as-plated, 350 °C-30-min and 400 °C-2-min samples. For XAS, background was removed using arc-tan function. XMCD were all normalized to XAS integration (r shown in Fig. 7). Arrows in (a) indicate the partial oxygen signals at Ni $L_{2,3}$ edges. Inset figure in (b) shows XMCD signals upon applied field reversal (±1 T) for the as-plated sample. Data shown in this figure were all taken at 30 K.

of Ni to form the clusters. The arrays are full of cluster boundaries, appearing mostly along the long axis. These boundaries are heterogeneous pathways, featuring low atomic density and large structural misfit which confine the FM domain rotation within the cluster. On the contrary, the electroplated arrays contain segmented and polycrystalline structures featuring microscopic shape anisotropy, as illustrated in Fig. 5. These structures greatly favor macroscopic shape anisotropy once the arrays' aspect-ratio is increased, resulting in effective magnetizing along the long axis.[27] However, such microscopic shape anisotropy is not seen in the electroless-plated arrays. We believe that the microstructural differences between the two plating-counterparts (Fig. 5) are responsible for the discrepancy in magnetic anisotropy, whereas additional efforts beyond this work are necessary to address the exact nature of the magnetic anisotropy of the electroless-plated arrays.

Figure 6(a) shows the x-ray absorption spectrum (XAS), and Fig. 6(b) shows XMCD data taken along arrays' long axis for the three samples. The arc-tan function was applied to the XAS to subtract the background noise. The XAS of each sample features satellite peaks around the main Ni L_2 and L_3 edges, suggesting the oxidation of the samples. The

oxidation probably took place during annealing, because the adjacent AAO may have served as an oxygen source to the Ni sample. Alternatively, it may have occurred when the arrays were exposed to the air. Nevertheless, the oxidation is partial, because the peak-splitting is less than that of the pure NiO sample.[14,28,29] This agrees fairly well with the atomic percentage of oxygen (∼20%) probed by EDX for all the samples. Both the line-shape and magnitude of the XAS vary insignificantly among the three samples. This rules out possible electronic modifications while the arrays undergo the SM→FM transition. The three samples' XMCD signals are superimposed in Fig. 6(b). A strong dependency of annealing condition, particularly at the L_2-edge, is observed. The largest XMCD signal is exhibited by the 400 °C-2-min sample, which indicates the strongest magnetization among the three samples, consistent with the SQUID results. The inset shows the XMCD reversal upon magnetic field reversal. Since helicity switching is equivalent to magnetization reversal, the reversal of XMCD signal in response to field switching is expected.

Nevertheless, the two opposite XMCD signals, as shown in the inset of Fig. 6(b), are not identical. Hence, sum-rules analysis was carried out independently for the data sets corresponding to the opposite applied fields, to account for systematic errors in the data. The analytical process, spectra background removal, integration ranges, and parameters (p, q, r) for sum-rules analysis are described in Fig. 7. The 3d electron occupation number, n_{3d}, used for calculating m_{orb} and m_{spin}, was set to 6 for all samples. Because the oxidation is only partial, no value of n_{3d} would accurately represent the electronic configuration of the Ni arrays. Setting n_{3d} to 8 (nonoxidized) instead of 6 also would have no effect on the *relative* change of m_{orb} or m_{spin}. Moreover, the quantitative determination of m_{orb} and m_{spin} can be affected by the substantial overlap between L_2 and L_3 edges, the details of background removal, or the sensitivity of TEY measurements. Therefore, the following discussion focuses on the *relative* changes in m_{orb} and m_{spin}.

The estimated m_{orb}, m_{spin}, and total magnetization ($m_{orb} + m_{spin}$) with respect to annealing temperature are demonstrated in Fig. 8. It clearly indicates that m_{spin} is larger than m_{orb} and that m_{spin} dominates the total magnetization. This is in reasonable agreement with other works related to nanostructured magnetism.[30,31] Interestingly, m_{orb} remains largely annealing-temperature-independent, whereas m_{spin} dominates the magnetization by increasing significantly with the increase in annealing temperature, which was noted as responsible for the magnetostructural SM→FM phase transition (Fig. 3). The sum-rules analysis here suggests that the spin-orbital coupling is insignificant during the phase transition. More importantly, the phase transition observed macroscopically is solely attributed to the change in m_{spin}.

The validity of the sum-rules analysis can be examined by comparing it with the SQUID results [Fig. 3(a)]. For H = 1 T and T = 30 K, sum-rules analysis shows that the 350 °C-30-min and 400 °C-2-min samples possess total magnetization larger than the as-plated sample by factors of 1.3 and 1.7, respectively. SQUID produced corresponding factors of 2.0 and 2.8, fairly confirming the consistency between
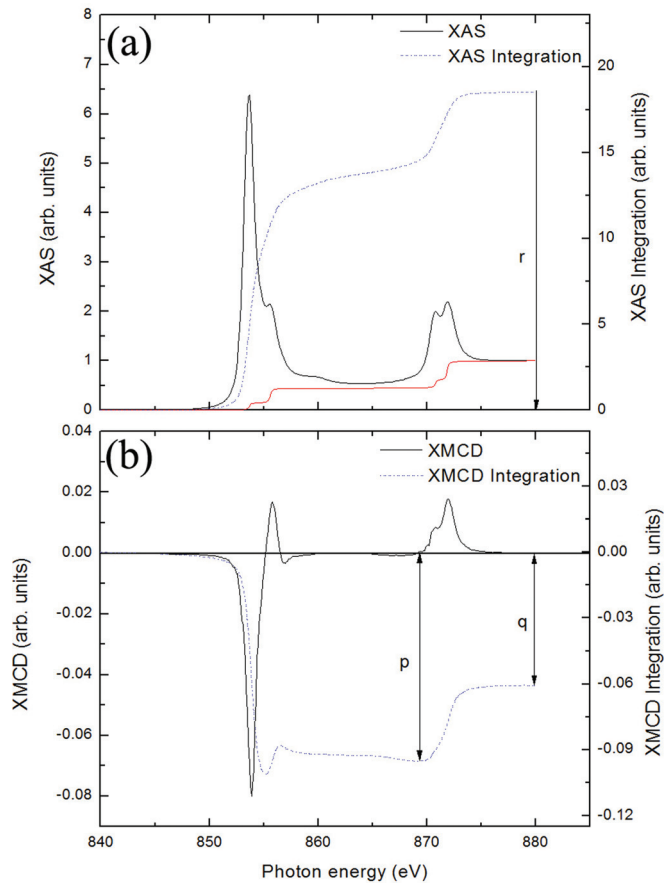
FIG. 7. (Color online) (a) XAS and (b) XMCD integrations applied in sum-rules analysis, taking the 400 °C-2-min sample as an example. In (a), the red line is the arc-tan background removal of the XAS spectrum. p, q, r are the three spectra integrations required in sum-rules analysis. More details of the sum rule analysis can be found in Ref. 13.

macroscopic and microscopic magnetic properties of the arrays. Although the XMCD for the short axis is omitted for brevity, the 400 °C-2-min sample shows that m_{spin} is also larger than m_{orb}, in accordance with that seen in the long axis measurements.

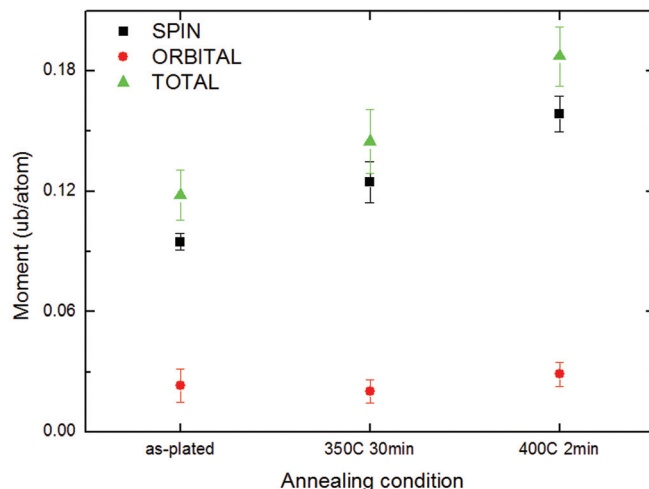In order to evaluate how thermal instability affects m_{orb} and m_{spin} for the as-plated sample in the SM phase, temperature-dependent XMCD (T = 30, 45, 55 K) and corresponding sum-rules analyses were carried out, as presented in Figs. 9(a) and 9(b), respectively. As expected, the XMCD signal decreased dramatically as temperature increased because of the loss of magnetization. Both m_{spin} and m_{orb} declined while temperature increased, suggesting a weakening spin-orbital coupling. The result indicates that m_{spin} is much more sensitive to temperature than is m_{orb}. It also suggests that m_{spin} is critical in determining both the loss and the enhancement of the total magnetization.

In summary, we have investigated the magneto-structural properties of the electroless-plated Ni nanoarrays in response to different annealing conditions. These properties were characterized using SEM, TEM, SQUID, and x-ray spectroscopy. It was found that the as-plated sample exhibits the SM phase as a result of nanocrystalline structure, inherent to electroless-plating. Post-annealing induced a magneto-structural SM→FM phase transition, where it restored the FM ordering by enhancing the crystallinity. Besides, the restoration of the FM ordering was proportional to the annealing temperature. Unlike the electroplated arrays, more effective moment saturation in the electroless-plated samples
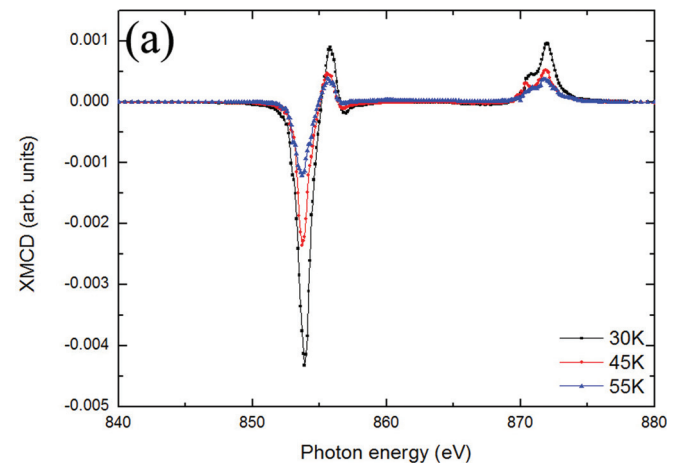

FIG. 9. (Color online) (a) Temperature-dependent XMCD for the as-plated Ni arrays. (b) Estimated m_{spin}, m_{orb}, and ($m_{spin} + m_{orb}$) as a function of temperature.

FIG. 8. (Color online) Estimated m_{spin}, m_{orb}, and ($m_{spin} + m_{orb}$) as a function of annealing condition.

was observed along the short axis than the long axis. This is attributed to the isolated cluster microstructures of the latter. The cluster isolation is speculated to hinder the moment alignment along a specific direction, which would explain the unusual magnetic anisotropy we observed. XMCD and sum-rules analysis provided a fundamental understanding of the annealing-induced phase transition. A remarkable increase in m_{spin} along with the increase in annealing temperature is observed, which dominates the change of magnetization. The domination of m_{spin} also is seen in temperature-dependent XMCD during the SM phase. These results suggest that microstructural ordering (crystallinity) and m_{spin} are the two essential factors in determining the magnetic properties of the electroless-plated Ni arrays.

ACKNOWLEDGMENTS

[1]Y. Park, S. Adenwalla, G. P. Felcher, and S. D. Bader, Phys. Rev. B **52**, 12779 (1995).

[2]F. C. Fonseca, G. F. Goya, and R. F. Jardim, Phys. Rev. B **66**, 104406 (2002).

[3]M. E. Mchenry and D. E. Laughlin, Acta Mater. **48**, 223 (2000).

[4]C. A. Ross, Annu. Rev. Mater. Res. **31**, 203 (2001).

[5]We define the term of "phase transition," in our case, to be the transformation of the Ni arrays from one magnetic state (superparamagnetic) to another (ferromagnetic) magnetic state. For both magnetic states, the system (arrays) has uniform physical properties, such as microstructure and magnetization. Thus, the term merely describes the different physical properties of the two magnetic states.

[6]T. K. Tsai and C. G. Chao, Appl. Surf. Sci. **233**, 180 (2004).

[7]Y. H. Cheng, Y. Zou, L. Cheng, and W. Liu, Mater. Lett. **62**, 4283 (2008).

[8]R. J. C. Brown, P. J. Brewer, M. J. T. Milton, J. Mater. Chem. **12**, 2749 (2002).

[9]C. M. Liu, Y. C. Tseng, C. Chen, M. C. Hsu, T. Y. Chao, and Y. T. Cheng, Nanotechnology **20**, 415703 (2009).

[10]R. Mogul, J. J. G. Kelly, M. L. Cable, and A. F. Hebard, Mater. Lett. **60**, 19 (2006).

[11]C. C. Lo, C. C. Huang, C. M. Liu, C. Chen, C. Y. Kuo, H. J. Lin, and Y. C. Tseng, J. Magn. Magn. Mater. **323**, 1950 (2011).

[12]We measured the raw M-H curve (1st) of the sample (Ni arrays on Si), and then removed the Ni arrays from the Si substrate by mechanical polishing. The remaining sample was examined by SEM to ensure the complete removal of the Ni, and then was sent to M-H (2nd) measurement again. We subtracted the second M-H (only Si) from the first M-H (Ni on Si) to ensure that the magnetic properties were contributed from the Ni alone.

[13]C. T. Chen, Y. U. Idzerda, H. J. Lin, N. V. Smith, G. Meigs, E. Chaban, G. H. Ho, E. Pellegrin, and F. Sette, Phys. Rev. Lett. **75**, 152 (1995).

[14]V. Corradini, F. Moro, R. Biagi, U. del Pennino, V. D. Renzi, S. Carretta, P. Santini, M. Affronte, J. C. Cezar, G. Timco, and R. E. P. Winpenny, Phys. Rev. B **77**, 014402 (2008).

[15]In our case, we define the "nanocrystalline" structure to be an array containing hundreds of crystals, with each crystal featuring a diameter of 2–3 nanometers. The micrograph of the nanocrystals can be acquired in Ref. 9. Because of the random orientations and the low microstructural ordering of these nanocrystals, it results in a diffusive and dull rim as demonstrated in Fig. 2(a).

[16]We define the "polycrystalline" structure to be an array containing hundreds of laminar grains, with each grain featuring ∼30 nanometers in length and ∼3 nanometers in diameter. These laminar grains tend to assemble together and to align along the long-axis of the arrays, as can be seen in Fig. 6 of Ref. 9. Because of its higher microstructure ordering than the nanocrystalline structure, the polycrystalline structure displays more order and brighter diffraction spots as demonstrated in Figs. 2(b) and 2(c)

[17]P. Allia, M. Coisson, P. Tiberto, F. Vinai, M. Knobel, M. A. Novak, and W. C. Nunes, Phys. Rev. B **64**, 144420 (2001).

[18]We used $M/M_0 = L(\mu H/k_B T)$ to run the Langevin fitting, where M/M_0 represents the normalized magnetic properties upon field application, $L(x) = \coth(x) - 1/x$, μ is the average magnetic moment for an individual nanocrystals, H is magnetic field, k_B is Boltzmann constant, and T is temperature. Here, we used $\mu = 4 \times 10^{19}$ emu) to fit the data. The value was estimated by dividing the moment to the number of nano crystals subject to the measurement.

[19]S. Z. Chu, K. Wada, S. Inoue, and S. I. Todoroki, Chem. Mater. **14**, 4595 (2002).

[20]F. Tian, J. Zhu, and D. Wei, J. Phys. Chem. C **111**, 12669 (2007).

[21]M. Vázquez, K. Pirota, J. Torrejon, D. Navas, and M. Hernandez-Velez, J. Magn. Magn. Mater. **294**, 174 (2005).

[22]Y. Gao, Z. J. Zheng, M. Q. Zeng, C. P. Luo, and M. Zhu, J. Mater. Res. **23**, 1343 (2008).

[23]P. S. Kumar and P. K. Nair, J. Mater. Process. Technol. **56**, 511 (1996).

[24]B. L. Young, J. G. Duh, and B. S. Chiou, J. Electron. Mater. **30**, 543 (2001).

[25]H. Pan, B. Liu, J. Yi, C. Poh, S. Lim, J. Ding, Y. Feng, C. H. A. Huan, and J. Lin, J. Phys. Chem. B **109**, 3094 (2005).

[26]H. Cao, C. Tie, Z. Xua, J. Hong, and H. Sang, Appl. Phys. Lett. **78**, 1592 (2001).

[27]S. L. Oh, Y. R. Kim, L. Malkinski, A. Vovk, S. L. Whittenburg, E. M. Kim, and J. S. Jung, J. Magn. Magn. Mater. **310**, 827 (2007).

[28]I. Preda, M. Abbate, A. Gutierrez, S. Palacın, A. Vollmer, and L. Soriano, J. Electron Spectrosc. Relat. Phenom. **156**, 111 (2007).

[29]D. Alders, L. H. Tjeng, F. C. Voogt, T. Hibma, G. A. Sawatzky, C. T. Chen, J. Vogel, M. Sacchi, and S. Iacobucci, J. Phys. Chem. B **57**, 11623 (1998).

[30]F. Tournus, N. Blanc, A. Tamion, P. Ohresser, A. Perez, and V. Dupuis, J. Electron Spectrosc. Relat. Phenom. **166**, 84 (2008).

[31]C. M. Teodorescu, Surf. Sci. **601**, 4292 (2007).